Alteration of Phase Transformation Behavior and Prior Austenite Grain Structure Due to Elevated Tramp Element Concentrations in a Hypoeutectoid Steel

Lukas Hatzenbichler, Marek Gocnik, Phillip Haslberger, Matthew Galler, Andreas Stark, Oleksandr Glushko, Jozef Keckes, and Ronald Schnitzer*

In order to reduce CO_2 emissions, the steel industry shifts its production toward the usage of higher scrap contents. This transformation leads to an elevation of tramp element concentrations, which can alter the steel's response during heat treatments. In this work, the phase transformation behavior of a hypoeutectoid steel grade is studied. A reference alloy from the blast furnace route is compared to alloys with increased tramp element concentrations. Dilatometry experiments are performed to obtain information about phase transformations. Additionally, the microstructure is examined with hardness measurements, optical as well as scanning electron microscopy including electron backscatter diffraction. Moreover, in situ high-energy X-ray diffraction measurements deliver information of the microstructural evolution during the heat treatment and provide a precise overview of the evolved phases after cooling. Finally, the prior austenite grain size is determined with a high-temperature laser scanning confocal microscope and is correlated to the observed phase transformation alterations. The examination of microstructures reveals that an increase in tramp element contents facilitates the formation of displacive phases along with retained austenite. Furthermore, it is observed that tramp elements impede the growth of prior austenite grains by segregating to the grain boundaries at high temperatures, thereby inducing a solute drag effect.

1. Introduction

The transition from blast furnace (BF) technology to an electric arc furnace (EAF) production route will enhance the utilization of scrap in steelmaking, resulting in an estimated reduction of CO_2 emissions by about 30%.[1] However, this greater reliance on scrap is expected to lead to higher concentrations of tramp elements. Studies on recycled steel have highlighted Cu, Cr, Si, Ni, Mo, As, Sn, Sb, Co, V, and Al as the most commonly occurring elements introduced from scrap.[2,3] While elements like Si and Al can be effectively removed through oxidation in secondary metallurgy, the extraction of others, such as Ni, Mo, As, Sn, Co, and particularly Cu, is extremely complex or even impossible.[4] Changes in chemical composition caused by these elements can possibly alter the behavior during heat treatments within the production process. As a consequence, the final microstructure and the corresponding mechanical properties are expected to be affected.[5] When present in solid solution, elevated levels of elements such as Cr, Mo, Cu, and Ni can shift the phase fields of a continuous cooling transformation (CCT) diagram to longer times and lower the critical cooling rate for displacive phases, therefore enhancing hardenability.[6] This leads to the assumption that higher concentrations of tramp elements promote displacive phase transformations, i.e., the formation of bainite or martensite.

Furthermore, it has been observed that some of the abovementioned tramp elements potentially segregate to the prior

---

L. Hatzenbichler, M. Gocnik, J. Keckes, R. Schnitzer
Christian Doppler Laboratory for Knowledge-based Design of Advanced Steels
Department of Materials Science
Montanuniversität Leoben
8700 Leoben, Austria
E-mail: lukas.hatzenbichler@unileoben.ac.at

The ORCID identification number(s) for the author(s) of this article can be found under https://doi.org/10.1002/srin.202500172.

DOI: 10.1002/srin.202500172

P. Haslberger
voestalpine Forschungsservicegesellschaft Donawitz GmbH
voestalpine AG
8700 Leoben, Austria

M. Galler
voestalpine Wire Rod Austria GmbH
voestalpine AG
8700 Leoben, Austria

A. Stark
Institute of Materials Physics
Helmholtz-Zentrum Hereon
21502 Geesthacht, Germany

O. Glushko
Department of Materials Science
Montanuniversität Leoben
8700 Leoben, Austria

austenite grain (PAG) boundaries and impede the grain boundary mobility, which is known as the solute drag effect.[7,8] Since the PAG size is a crucial parameter influencing the microstructure evolution during subsequent cooling, grain refinement may have multiple effects.[9] The PAG boundaries serve as nucleation sites during phase transformations. A smaller PAG size provides larger grain boundary area, which leads to a higher density of nucleation sites and faster phase transformation kinetics, particularly for pearlite.[10] However, in a study on a hypoeutectoid steel by Aranda et al.[11] it was reported that larger PAGs result in a higher volume fraction of pearlite due to the absence of nucleation sites for proeutectoid ferrite. Moreover, it is also known that segregated elements can suppress the nucleation and growth rate of ferrite and pearlite.[12,13]

Considering displacive phase transformations, it has been found that the martensite formation rate increases with smaller austenite grains during the first degrees of undercooling below the martensite start temperature.[14] However, by observing the entire transformation process, displacive transformation in general should be enhanced by a larger PAG size and take place already at lower cooling rates.[15] Another perspective is that a smaller PAG size lowers the M_s temperature by stabilizing the austenite phase, leading to faster martensitic transformation kinetics due to enhanced driving forces at higher undercooling.[16–18]

Despite extensive research on phase transformations, the specific role of tramp elements for the microstructural development of modern advanced steels with complex hierarchical structures is not fully understood yet. These steels were developed relying on steel production processes resulting in very low amounts of tramp and trace elements. Therefore, existing studies primarily focus on alloying elements, while the effects of tramp elements are less explored. However, this knowledge is of great importance for maintaining the steel's quality throughout the transformation to a CO_2-reduced steel production with high recycling rates.

Consequently, in this work, the impact of tramp elements on the phase transformation behavior of a hypoeutectoid wire rod steel grade is investigated and the resulting microstructure is characterized by the utilization of advanced methods. Additionally, the PAG size at high temperatures is quantified. Its potential impact on phase transformations is thoroughly assessed. The study aims to provide new insights into how tramp elements and prior austenite grain size shape the microstructural evolution, ultimately contributing to a deeper understanding of steel processing and performance.

2. Experimental Section

2.1. Alloying Concept

A hypoeutectoid wire rod steel was utilized to study the influence of tramp elements on the phase transformations during heat treatments. The reference alloy was produced via the BF route and compared to trial alloys casted with increased concentration of tramp elements. These alloys imitate the EAF steel production and its increased scrap usage. The elevation of tramp elements was estimated once at a medium level and once at a high level of tramp elements. The main alloying elements of the three alloying variants are shown in **Table 1**.

Table 1. Main alloying elements of the investigated wire rod steel grade for the reference alloy from BF and the trial alloys with increased levels of tramp elements.

Alloying variants	[wt%]		
	C	Si	Mn
Reference	0.62	0.27	0.64
Medium level	0.62	0.25	0.64
High level	0.62	0.26	0.65

Table 2. The elevation of tramp element concentrations relative to the reference alloy for the trial alloys in its medium level as well as high level variants.

Alloying variants	[Δppm]								
	Cr	Ni	Cu	Mo	Sn	Co	P	S	N
Medium level	280	340	510	140	60	–	–	–	–
High level	600	730	940	380	280	80	40	–	40

In **Table 2**, the deviation of the tramp element contents relative to the reference alloy is displayed. In the alloy with a medium level of tramp elements, Cr, Ni, Cu, Mo, and Sn were elevated, while in the alloy with a high level of tramp elements, Co, P, and N were additionally increased.

2.2. Heat Treatment

The heat treatment shown in **Figure 1** was applied on all three alloying variants. The evolved microstructures after the heat treatment, including cooling with 10 °C s^{-1} were analyzed to gather information about the present phases. Additionally, the same heat treatment was performed while exposing the material to a high-energy X-ray diffraction (HE-XRD) beam, allowing the phase evolution to be monitored throughout the entire temperature range. Furthermore, the PAG size after a holding period of 10 min at 1100 °C was determined for all investigated alloys.

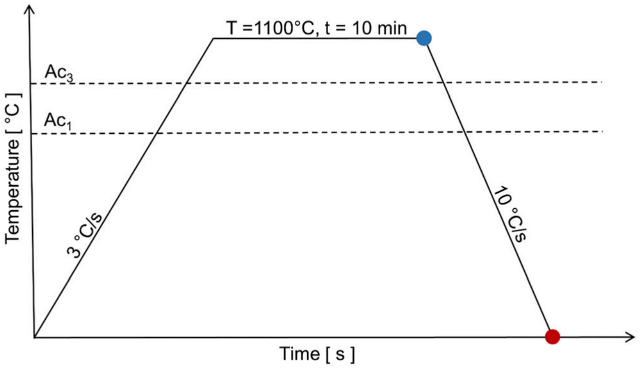

Figure 1. Heat treatment was applied to the investigated alloys. The microstructures are examined after the heat treatment (red point), and the PAGs are analyzed at 1100 °C after a holding period of 10 min (blue point).

2.3. Dilatometry

Dilatometry samples with a length of 10 mm and a diameter of 5 mm were machined from the center of the straightened wire rods. They were heat-treated in a quenching dilatometer DIL805A (TA Instruments) with an inductive heating system. All heating cycles were performed under vacuum conditions. Helium was used as a cooling agent. The temperature was measured with a type S (Pt-Pt10Rh) thermocouple at the surface of the samples. The phase transformation temperatures were determined from the dilatometry curves using the tangent method.[19]

2.4. Microstructural Analysis Techniques

The longitudinal sections of the heat-treated specimens were examined with a Zeiss Axio Imager M2 optical microscope (OM) after Nital etching (3% HNO_3 in ethanol). This etching technique provided clear contrast between the present phases and hence, it was possible to determine the fraction of displacive phases in the material by using stereological analysis. OM images were evaluated within the integrated ZenCore software following the ASTM E 112-13 standards.[20] To gain deeper insight, the microstructure of the same samples was investigated using a Tescan Clara scanning electron microscope (SEM) equipped with an electron backscatter diffraction (EBSD) detector from Oxford Instruments. The SEM images of the etched microstructure were taken in secondary electron mode, working at an acceleration voltage of 10 kV. The samples for EBSD analysis required electropolishing in order to obtain reliable patterns. The measurements were performed using a working voltage of 20 kV and a step size of 60 nm. For the EBSD measurements of the quenched microstructure, in order to reconstruct the PAGs and estimate the grain size in the bulk, a step size of 250 nm was used. The data analysis was done with the Aztec Crystal software provided by Oxford Instruments.

Hardness measurements were conducted with a QNess Q10 A + from QATM. A Vickers indenter was used with a force of 98.1 N (HV10); otherwise, the standard parameters for Vickers hardness testing were used.[21] The mean values of the hardness represent the average of ten indents distributed over the polished sample surface.

2.5. In Situ High Energy X-ray Diffraction

HE-XRD experiments were conducted at the P07 beamline at PETRA III of Deutsches Elektronen-Synchrotron (DESY) in Hamburg, Germany. In situ measurements were conducted via a customized dilatometer integrated in the beamline. The preparation of the dilatometer samples, the temperature measurements, and the heat treatment conditions were performed in the same way as described in section 2.3. Samples were irradiated with monochromatic X-ray radiation with an energy of 87.1 keV ($\lambda = 1.4235$ nm) collimated to a size of 0.2×0.2 mm. Prior to the measurements, the experimental configuration was calibrated on a NIST (National Institute of Standards and Technology) standard LaB_6 powder (SRM 660b). Resulting 2D diffraction patterns were subsequently radially integrated in PyFAI-based software[22] to obtain 1D 2Θ-intensity diffractograms.

2.6. High-Temperature Laser Scanning Confocal Microscopy

The phase transformations and PAGs are additionally investigated in situ utilizing a high-temperature laser scanning confocal microscope (HTLSCM, VL2000DX-SVF17SP-Yonekura). This experimental setup enables the application of a specific heat treatment to a sample material while simultaneously monitoring the surface continuously. PAGs become visible through thermal etching at elevated temperatures. Additionally, phase transformations during cooling can be visualized, i.e., the formation of martensite. The heating of the sample surface works with an infrared furnace and the simultaneous imaging with a violet laser diode (408 nm) providing an excellent depth resolution. A vacuum in the chamber is created, and subsequently it gets purged with Ar to achieve a neutral atmosphere for operation. With additional He supply, cooling rates up to 100 °C s^{-1} can be achieved.

3. Results

3.1. Influence of Tramp Elements on Microstructural Development

The microstructures of the materials in their initial condition before and after the heat treatment (shown in Figure 1) were examined using OM. The initial microstructures of the three alloying variants all consist of pearlite with a small amount of grain boundary ferrite (**Figure 2**a–c). No significant differences were observed at this resolution. However, clear changes are evident when comparing the microstructures after the heat treatment (Figure 2d–f). In addition to the ferritic-pearlitic microstructure, a second microstructural constituent developed, which is appearing bright under the OM. These bright regions are attributed to martensite as it is known to be less attacked by the used etchant (Nital). Based on this observation, the trend shows an increasing fraction of martensite, starting from the reference material (≈0.1%), followed by the alloy with a medium level (≈1.2%), and then the alloy with a high level of tramp elements (≈7%). The observed differences in the microstructure suggest that even the relatively low amount of tramp elements promotes the formation of displacive phases.

The cooling curves of the dilatometry measurements at a cooling rate of 10 °C s^{-1} are illustrated for the investigated alloy variants in **Figure 3**a. A detailed analysis in Figure 3b reveals that as the concentration of tramp elements increases, the austenite-to-pearlite transformation shifts progressively to lower temperatures. A difference of about 38 °C is observed for the start of austenite decomposition between the reference alloy and the trial alloy with a high level of tramp elements. This behavior indicates that tramp elements significantly influence the transformation kinetics. In Figure 3c it is shown that the martensite start temperature (M_s) remains consistent in a range of ± 5 °C across the different alloying variants, suggesting that the addition of tramp elements does not significantly alter the onset of martensite formation in this case. However, a notable difference in the curvature of the cooling curve is observed in the alloy with a high level of tramp elements. This distinct curvature change is indicative of a higher martensite fraction in this alloy, further confirming the impact of increased tramp element concentrations on the

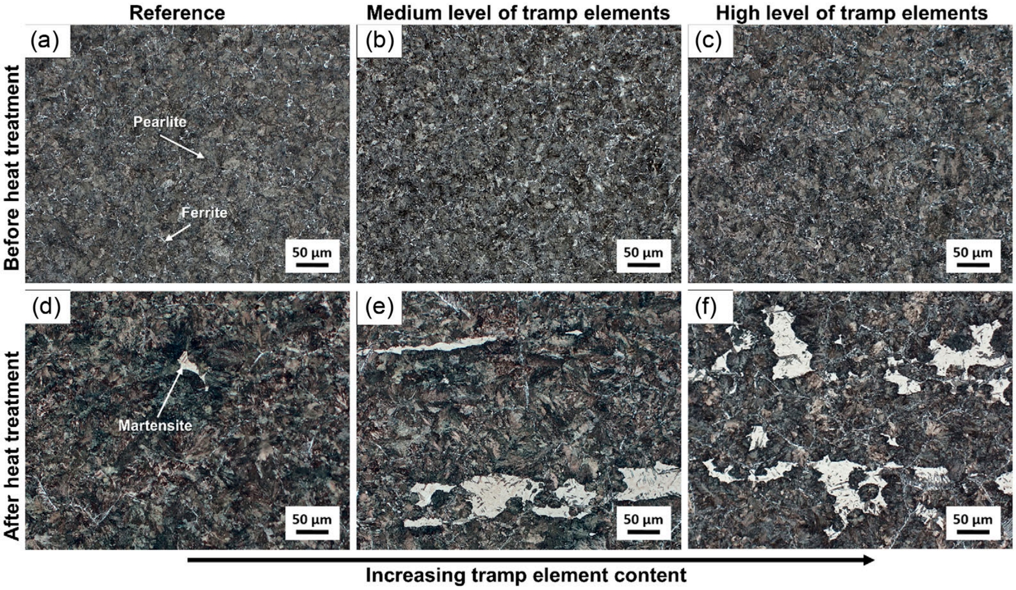

Figure 2. In a–c) OM images of the initial states before the heat treatment for the reference alloy and the trial alloys with medium and high levels of tramp elements, respectively, are presented. All of them exhibit a pearlitic microstructure with grain boundary ferrite. The microstructures after the heat treatment with a cooling rate of 10 °C s^{-1} again for d) the reference alloy, e) the alloy with medium level, and f) the alloy with high level of tramp elements are shown. In this case, the martensite fraction increases from the reference material to the alloy with a high level of tramp elements, indicating a correlation with the amount of tramp elements present.

transformation behavior and the hardenability of this steel grade. According to existing CCT diagrams, bainite is also expected to form at a cooling rate of 10 °C s^{-1}.[23] However, its fraction appears to be too low to be distinctly identified in both the OM images and the dilatometry curves.

To validate the observed changes in microstructure through mechanical properties, hardness measurements were performed. The results presented in **Figure 4** indicate that an increase in hardness is already evident before the heat treatment is applied, which can be attributed to a solid solution strengthening effect. Furthermore, the higher measured hardness of the trial alloy with higher hardness after the heat treatment reflects the higher fraction of martensite as well as the more pronounced solid solution strengthening effect due to the increasing concentration of tramp elements. In absolute values, an increase of about 35 HV is measured by comparing the reference alloy and the trial alloy with a high level of tramp elements, whereas the difference was much smaller before the heat treatment (≈15 HV). The trial alloy with medium level of tramp elements lies right in the middle of the other two alloys in both cases.

Further inspection of the evolved microstructural constituent after the heat treatment were carried out with SEM and EBSD for the trial alloy with high level of tramp elements. A highly magnified OM image was captured (**Figure 5**a), where specific features were selected (marked with blue rectangles) for detailed examination in SEM. Primarily, a dark microstructural constituent in the center of a martensitic island was visualized in the SEM (Figure 5b). While cementite usually appears bright in SEM, ferrite can be identified as the dark phase (vice versa to bright-field OM images). Therefore, this microstructural constituent is identified as bainite, characterized by ferrite plates and interplate carbides, as described by Bhadeshia for upper bainite.[24] In Figures 5c–d, sharp interfaces between the individual constituents are depicted. The SEM images reveal that the pearlite, which surrounds the martensite islands, does not exhibit a typical lamellar structure but instead forms in a degenerated manner.[25] The martensite is only slightly affected by the etchant, but its block-like structure is still clearly visible in the SEM images and distinguishable from pearlite and bainite. Figure 5e illustrates a second type of bainite, characterized by a smooth transition from the area where pearlite is present. This bainite grows as a bundle of ferrite and carbide plates, extending into the martensitic island. In summary, the microstructure is determined as martensite combined with small amounts of upper bainite surrounded by degenerated pearlite.[25]

When cooling a steel with 0.6 wt.% at relatively high rates, retained austenite (RA) can also be expected within the microstructure, since the M_f temperature lies below room temperature (RT).[26] This is the reason why a martensitic island of the alloy with a high level of tramp elements was further investigated with EBSD. In order to localize the region of interest for EBSD characterization, the martensitic regions were first identified using the backscattered electron (BSE) detector (**Figure 6**a). In the inverse pole figure (IPF) map (Figure 6b), fine martensite blocks are visible exhibiting nearly identical orientations. Bainitic sheaves and surrounding pearlite can also be identified, according to the labels of Figure 6b. In Figure 6c, the phase map of the measurement is represented, showing that most of the microstructure is identified as a body-centered cubic (BCC) crystal structure. However, RA in form of small islands between the martensite blocks or at the edges of bainite sheaves was also detected. Therefore, it can be concluded that tramp elements

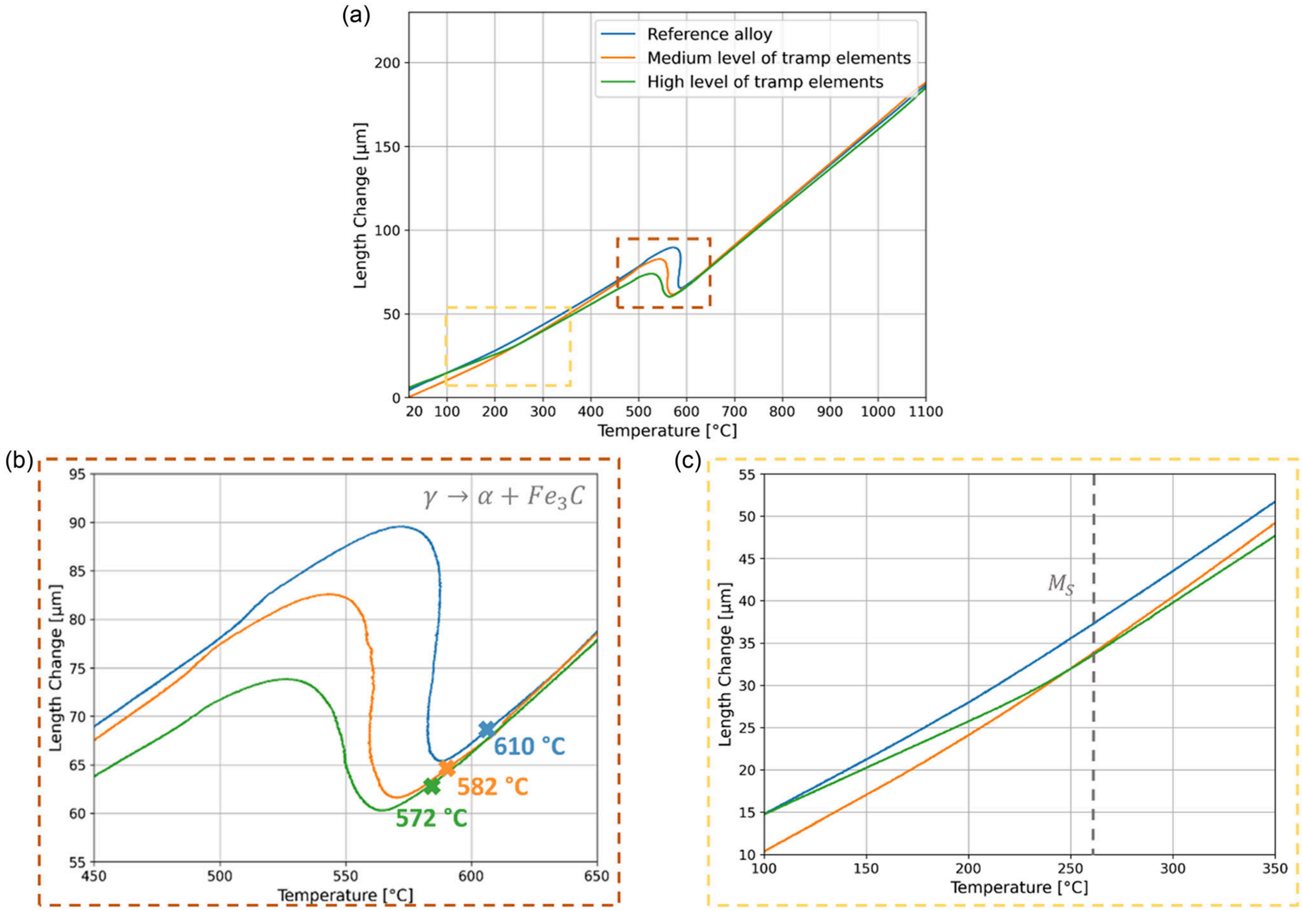

Figure 3. Dilatometry cooling curves for a cooling rate of 10 °C s^{-1} for the investigated alloys are presented in a). Panel b) shows the enlarged region of the austenite-to-pearlite transformation ($\gamma \rightarrow \alpha + Fe_3C$), which shifts to lower temperatures as the concentration of tramp elements increases. Panel c) depicts the enlarged region around M_s temperature. The curvature below M_s shows a distinct change only for the alloy with a high level of tramp elements, confirming the presence of a higher martensite fraction.

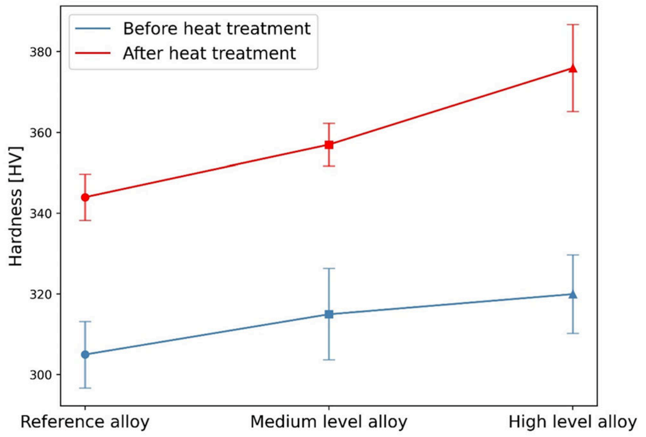

Figure 4. The hardness of the investigated alloys before and after the heat treatment. A noticeable trend of increasing hardness with the addition of tramp elements is evident even prior to the heat treatment. This trend becomes more pronounced in the heat-treated samples exposed to a cooling rate of 10 °C s^{-1}.

not only increase the fraction of displacive phases but also contribute to the presence of RA within these phases. In conclusion, the island-like displacive microstructural constituent of the trial alloy with high level of tramp elements contains not only martensite, but also small fractions of bainitic sheaves as well as RA.

3.2. Phase Development During Heat Treatment

The phase evolution during the heat treatment was investigated for the three alloying variants in detail by in situ HE-XRD. Using this technique, the beam continuously interacts with the material subjected to a heat treatment (**Figure 7**a) in a dilatometer, while the detector records the diffraction intensities.[27] Those intensities can be displayed in the form of a diffractogram, as for example shown in Figure 7b for the reference material. At RT, distinct ferrite (α) peaks can be observed, along with some faint cementite peaks (all peaks not indicated as α or γ) originating from the cementite lamellae in pearlite. Upon reaching the A_{C3} temperature, the microstructure transforms into austenite (γ) and remains stable during the holding period at 1100 °C. For the

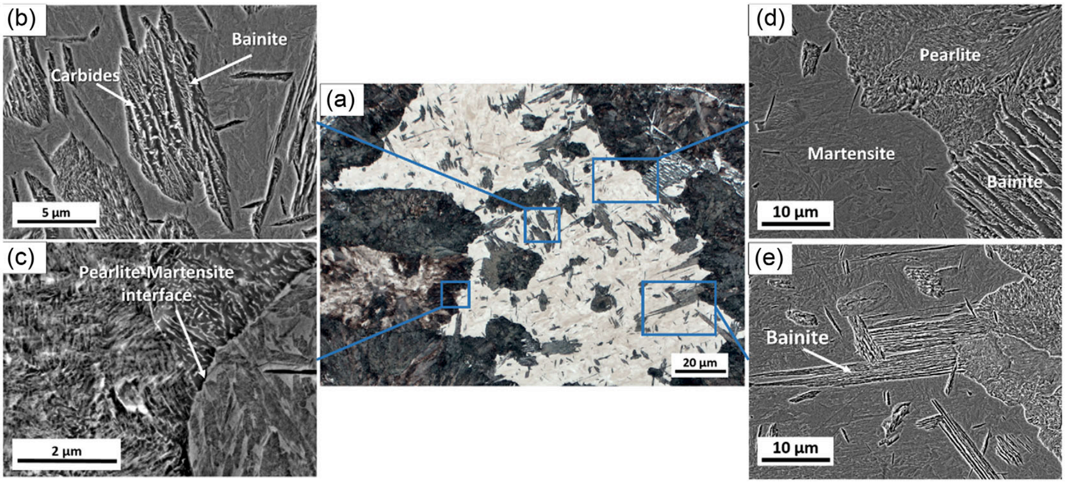

Figure 5. In a) an OM image of a martensitic region is shown. In b–e) certain areas, marked with the blue rectangles, are examined more in detail in the SEM.

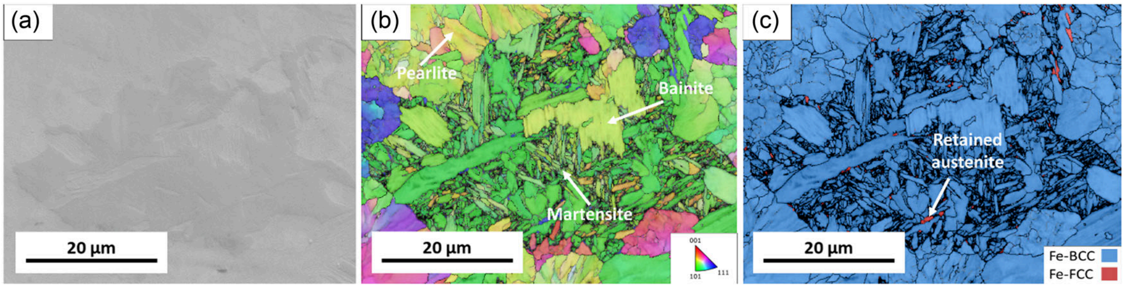

Figure 6. a) SEM image of a region containing displacive microstructural constituents, b) the corresponding IPF grain orientation map, and c) the phase map of the same area.

reference material, the microstructure appears to revert to its initial state during cooling down to RT. From the microstructural characterizations in the previous sections, it is already known that displacive phases, along with RA, evolve at this cooling rate. However, distinguishing martensite and bainite from ferrite or pearlite on the basis of XRD data is challenging and the RA content appears to be too low to be detected here. By comparing the diffractogram with those of the trial alloy with a medium level (Figure 7c) and the one with a high level of tramp elements (Figure 7d), it can be also observed from the HE-XRD data that all alloys consist of the same microstructure before the heat treatment. Furthermore, throughout the holding process, no unexpected changes are observed in the alloys with elevated tramp element content, which assures that all three alloy variants start with a fully austenitized microstructure prior to cooling. After cooling, the alloy with medium level of tramp elements shows the same pattern of peak intensities as the reference alloy. However, for the alloy with high level of tramp elements, it appears that, in addition to the ferrite and cementite peaks, faint austenite peaks persist until RT, which further indicates the presence of RA.

The comparison of the conditions before and after the heat treatment in **Figure 8**a–c reveals that the peak patterns for the reference alloy align quite well. In contrast, for the trial alloys with medium and high level of tramp elements, the peaks at the diffraction angles corresponding to the austenite peaks become increasingly prominent in the diffractograms after the heat treatment. For the magnified diagrams around the γ-200 peak (Figure 8d–f), it is evident that the intensity of this peak in the alloy with high level of tramp elements is much stronger than in the reference alloy or in the alloy with medium level of tramp elements. In the medium level alloy, the peak intensity remains insufficient to determine a reliable absolute value for the RA content and is likely close to zero. Conversely, for the alloy with a high concentration of tramp elements, the RA content is calculated to be ≈1.5% after the heat treatment. This is a further confirmation that displacive transformation is promoted by the addition of tramp elements, as RA forms alongside martensite. Therefore, the greater the amount of displacive transformation, the more RA occurs, even if the same heat treatment is applied.

3.3. In Situ Observation of Phase Transformations and Prior Austenite Grains with HTLSCM

Finally, a HTLSCM was utilized to follow the development of microstructure during the heat treatment. The advantage of this experimental setup is that it allows in situ monitoring of phase transformations during cooling as well as the growth of PAGs at high temperatures by recording a video of the sample's surface.

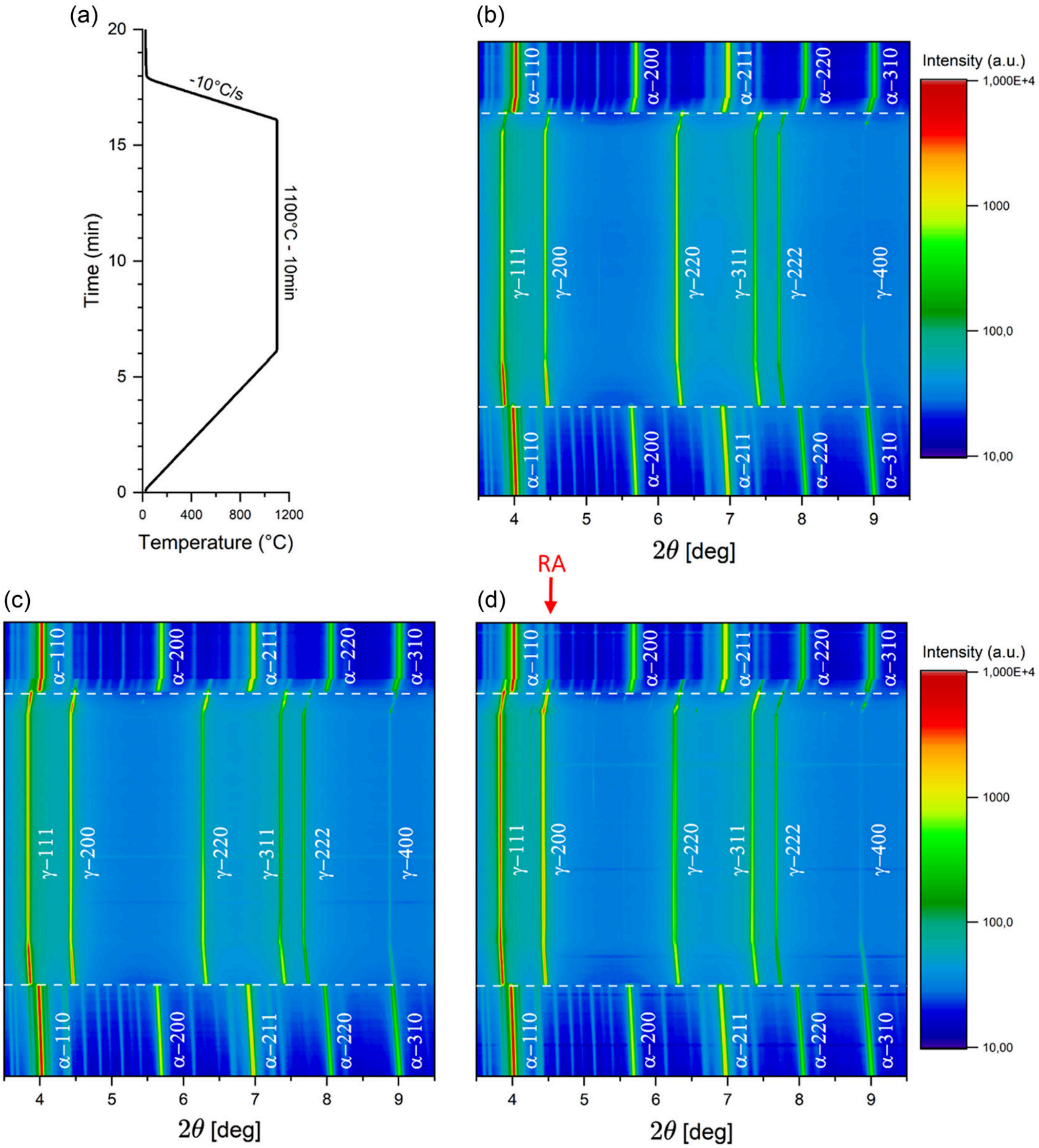

Figure 7. In a) the applied heat treatment in the dilatometer during the in situ HE-XRD measurement is shown, which can be directly correlated to the corresponding diffractograms from HE-XRD for b) the reference alloy, c) the trial alloy with medium level, and d) the alloy with high level of tramp elements. Between the reference and the alloy with medium level, no differences in the peak intensity patterns are observed here; both show ferrite (α) and cementite peaks before and after heat treatment at the expected diffraction angles 2θ. In the alloy with a high level of tramp elements faint austenite peaks (γ) are detected, most prominent for the γ-200 peak, after the heat treatment indicating RA.

The PAGs become visible due to thermal etching of the grain boundaries as it is shown in **Figure 9**a–c. These images show the PAG structure at 1100 °C after the holding period of 10 min. The size of these PAGs is crucial for the subsequent phase transformations during the cooling process. Additionally, the formation of bainite and martensite can be observed due to their different formation temperatures. It can be observed that bainite grows in sheaves, which form around 420 °C, directly from the PAG boundaries. The martensite first appears at around 250 °C (M_S) in an irregular manner. The observed M_S temperature aligns well with the value obtained from dilatometry (see Figure 3). The final images at RT are demonstrated in Figure 9d–f. Here, the surface after cooling at a rate of 50 °C s^{-1} is shown. Significant amounts of bainite and martensite, which appear dark in the images, can be clearly detected already for the reference alloy at this cooling rate as shown in Figure 9d. With increasing amount of tramp elements even higher fractions of the surface is covered by the displacive microstructure, as follows from Figure 9e and Figure 9f. The videos directly showing the differences in phase transformation kinetics for the three alloys are available as Supporting Information.

Furthermore, the thermally etched PAGs directly before cooling are analyzed more in detail. In order to calculate the area of

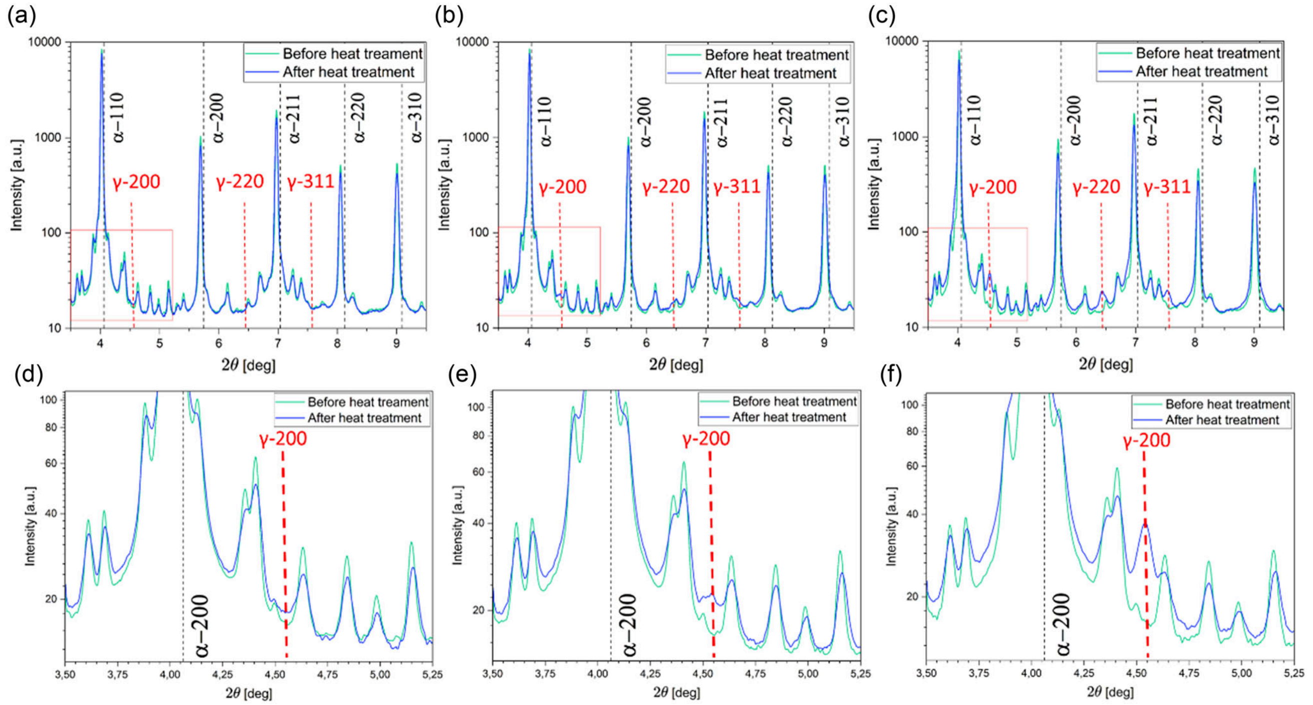

Figure 8. The diffractograms of the microstructure before and after the heat treatment for a) the reference, b) the trial alloy with a medium level, and c) with a high level of tramp elements. Panels d–f) display the magnified diagrams at the positions of the red rectangles, respectively. It can be seen that the intensities of the austenite (γ) peaks increase with the addition of tramp elements after cooling with 10 °C s^{-1}, confirming the presence of RA.

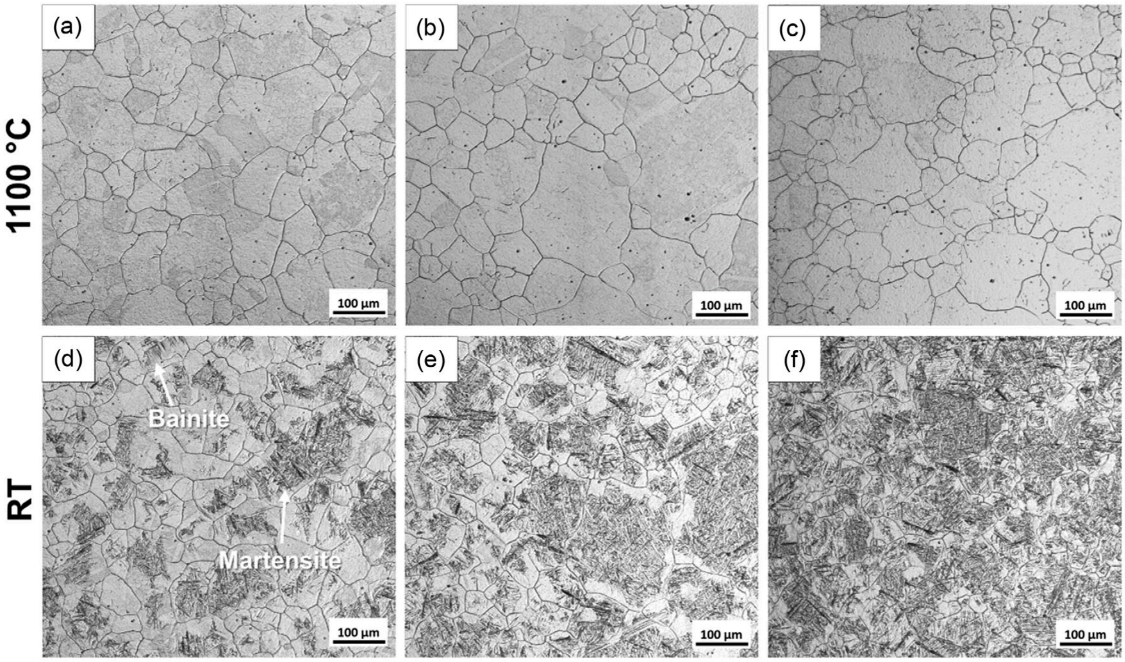

Figure 9. The PAGs for a) the reference, b) the alloy with medium level, and c) the alloy with high level of tramp elements are shown after a holding period of 10 min directly before cooling. Panels d–f) show the sample surfaces at RT after cooling at 50 °C s^{-1} for the three alloys, respectively, illustrating the trend of the investigated steel grade toward higher martensite fractions.

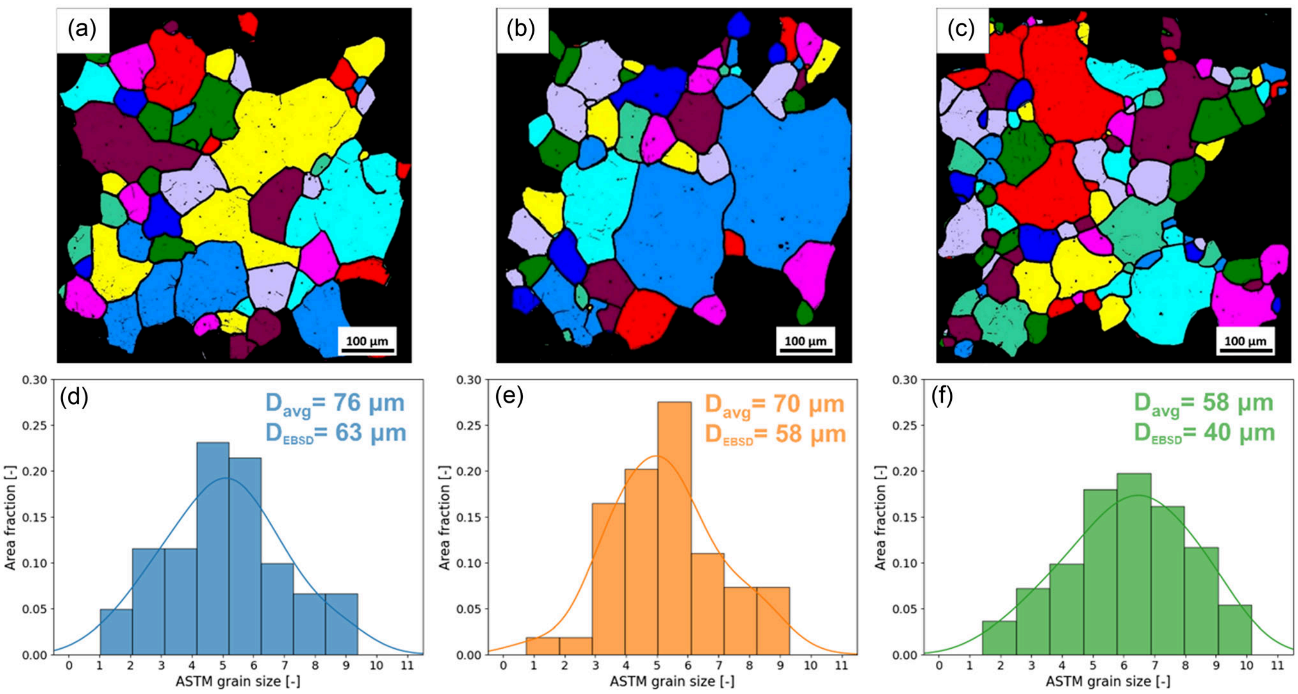

Figure 10. The evaluated PAGs are presented for a) the reference alloy, b) the alloy with a medium level, and c) the alloy with a high level of tramp elements after a 10 min holding period. The corresponding grain size distributions as well as the average grain diameters from HTLSCM (D_{avg}) as well as from EBSD (D_{EBSD}) are directly below these images in panels d–f). Additionally, a kernel density estimation fit[49] (solid line) is applied to the distributions for better visualization.

each grain, the black grain boundaries are recognized by OpenCV image analysis modules[28] utilized within a Python code. The recognized grains are marked with random colors for better visualization (**Figure 10**a–c). It is important to exclude grains, which pass over the image edge as they would distort the average grain size. The corresponding ASTM grain sizes as well as the diameters are calculated as described in ASTM E112.[20] From this planimetric grain analysis, an average grain size as well as a grain size distribution is obtained (Figure 10d–f). It has been found that the average diameter, D_{avg}, of the PAGs decreases with the elevation of tramp element concentration. For the alloy with high level of tramp elements, a decrease by 18 µm in comparison to reference alloy has been determined. By comparing the grain size distributions, it appears they shift toward higher ASTM grain size numbers, indicating smaller grain sizes, progressing from the reference through the alloy with medium level to the alloy with high level of tramp elements. Even to the naked eye, it is evident that the fraction of small grains increases in the alloy with a high level of tramp elements, indicating a tendency toward abnormal grain growth. Consequently, the average grain size values do not fully capture this difference. The distinction becomes even more pronounced when comparing the grain size distributions.

To validate the HTLSCM measurements, EBSD analyses were performed on quenched microstructures, and prior austenite grains were reconstructed. The reconstructed grain sizes were found to be slightly smaller than those obtained via HTLSCM, but the trend regarding the tramp elements has been found to be correct, as indicated by the average diameters (D_{EBSD}) in Figure 10. This confirms that the trend to smaller, prior austenite grain sizes observed at the surface by thermal etching, is representative of the bulk microstructure as validated by consistent results from the alternative method and corroborated by findings reported in the literature.[29–31] Moreover, thermal etching proved highly effective for this material, with minimal evidence of ghost traces observed. Moreover, no discernible surface distortion appears to have affected the accuracy of the measurements.

4. Discussion

While phase transformations in steels have been widely studied, the influence of tramp elements, such as Cu, Sn, and Co on the microstructural evolution of advanced steels remains insufficiently understood. Moreover, conventional alloying elements such as Cr, Ni, and Mo, when unintentionally introduced through scrap, can also induce significant alterations in the microstructural development of low-alloyed steels. The gap of this knowledge stems from the fact that the development of these steels has traditionally relied on production routes that minimize the presence of tramp and trace elements. As a result, prior research has predominantly concentrated on the role of intentional alloying elements, however, the importance to understand the effects of unintended residuals get more important for the transition to scrap-based steel production. In the present study, this critical issue is addressed through a systematic investigation of the effects of tramp elements on microstructural evolution. The resulting insights are comprehensively analyzed and discussed in the following sections.

4.1. Promotion of the Formation of Displacive Phases by Tramp Elements

It is well established that elements such as Cr and Mo enhance the hardenability of steels by shifting the transformation kinetics in CCT diagrams toward longer timescales.[6] This phenomenon has been predominantly documented at concentrations above 1 wt% while its effects at lower concentrations, specifically below 0.1 wt% (as in the alloys investigated in this study), remain less thoroughly explored. However, it is important to note that other tramp elements such as Cu and Ni are inducing similar effects like Cr and Mo on hardenability.[6] Thus, it is likely that the cumulative presence of tramp elements drives the microstructural changes observed after heat treatment, as illustrated in Figure 2d–f. In particular, the alloy with a high level of tramp elements exhibits an increased fraction of displacive transformation products, ≈7% higher compared to the reference alloy.

This trend is further corroborated by the results of the corresponding hardness measurements, which are shown in Figure 4. The observed increase in hardness can be attributed to the higher volume fraction of displacive phases after the heat treatment. However, even in alloys exhibiting purely pearlitic microstructures, a measurable increase in hardness is evident. This suggests a solid solution strengthening effect induced by the tramp elements. Hence, the mechanical response of the alloys with increased levels of tramp elements appears to result from a synergistic contribution of both solid solution strengthening and the increased fraction of displacive transformation products. The solid solution strengthening effect must also be considered in relation to phase transformations, as it may influence the nucleation conditions for martensite, as outlined by Ghosh and Olson.[32] These observations suggest a more complex interplay between chemical composition and transformation kinetics than previously assumed, challenging the traditional focus on higher-concentration effects. Further supporting this, a decreased interlamellar pearlite spacing, likely driven by minor Cu, Mo, and Cr additions, could enhance strength that has been mostly recognized at higher concentrations as well.[33,34]

In general, increasing the concentration of certain elements is also intended to modify the stability range of austenite and thereby influence its decomposition behavior. In the case of austenite stabilizers, this results in the formation of transformation products at lower temperatures. The lower transformation temperature significantly reduces the diffusion mobility of carbon and other elements. Consequently, the formation of diffusion-controlled microstructures such as pearlite is suppressed, while the transformation to harder, displacive structures like bainite or martensite is favored.[35] This interpretation is consistent with the experimental observations for the investigated alloys containing elevated levels of tramp elements, where an increase in tramp element concentration (particularly of austenite-stabilizing elements such as Cu, Ni, Co, and N[35,36]) corresponds to a reduction in the pearlite transformation temperature (Figure 3). Therefore, this observation can once again be correlated with the increased fraction of displacive phases in alloys containing higher levels of tramp elements.

Furthermore, elevated levels of RA observed via HE-XRD (Figure 8) underscore the role of tramp elements in modulating phase stability. It is reported by Pierce et al.[37] that not only Cr, but also Ni, decelerate the kinetics of austenite decomposition, leading to higher amounts of RA. The stability of RA in TRIP steels also appears to improve with Cu additions.[38] This aligns well with the observations in this work, as Cr, Ni, and Cu concentrations are increased in the alloys with medium and high levels of tramp elements, in which rising RA content has been detected. Hence, the findings of this study complement existing studies, but extend their relevance into previously unexplored compositional ranges.

Another important factor to consider is the segregation of certain elements to prior austenite grain boundaries, which can suppress pearlite nucleation, a phenomenon predicted by Yan et al.[12] via computational modeling. However, also experimental evidence has shown that for example Cu reduces the grain boundary energy of austenite, thereby decreasing both the nucleation rate and growth kinetics of ferrite.[13] Another tramp element, prominent for segregation and particularly temper embrittlement of steel, is Sn.[39,40] With increasing Sn content, and the associated enhanced segregation, significant microstructural changes are observed during the austenite-ferrite transformation. Specifically, the pearlite fraction decreases, and instead of forming polygonal ferrite, the microstructure exhibits a higher prevalence of Widmanstätten ferrite.[41] These findings further support the notion that tramp elements promote displacive transformation mechanisms at the expense of diffusional phase formation. Hence, it is also demonstrated how tramp elements, particularly Sn and Cu, could affect grain boundary chemistry and phase nucleation kinetics. Together, these findings illustrate that even trace amounts of tramp elements can have outsized effects on microstructure evolution, warranting greater consideration in steel design.

4.2. Refinement of Prior Austenite Grains Due to Solute Drag

The segregation of tramp elements to the PAG boundaries could influence phase transformation not only directly, but also indirectly by decreasing the prior austenite grain size due to impediment of the grain boundary mobility. This phenomenon is referred to as the solute drag effect, which is confirmed when an increase in solute concentration leads to a retardation of grain boundary movement and, consequently, inhibits grain growth.[7] This study reveals a clear solute drag effect associated with tramp elements, leading to substantial refinement of PAGs (Figure 10). A reduction in PAG size is observed with increasing concentrations of tramp elements. In this context, P and Sn are of particular importance, as they are among the most prominent elements known to segregate to grain boundaries. Therefore, they are significantly contributing to the refinement of the austenite grain structure, as previously reported in the literature.[8,42] While grain refinement is generally associated with accelerated pearlite transformation due to increased nucleation sites,[12] the data of this study shows that in alloys with high tramp element content, despite their smaller PAG sizes, displacive transformation is actually favored. This suggests that the observed reduction in PAG size (approximately by 20 µm when comparing the reference alloy to the alloy with a high level of tramp elements) has a relatively minor effect on the phase transformation behavior compared to the more pronounced influence of changes in chemical composition. This indicates that the influence of elements such as Cu and Sn on PAG boundary energy plays a significantly greater role in altering phase transformation behavior than the effect of the PAG size itself.

However, the refinement of PAGs also leads to a stabilization of the austenitic phase, which could contribute to the decrease of the pearlite transformation temperature. Moreover, a consequent reduction of M_S temperature is expected, which accelerates the transformation kinetics of martensite.[17] However, as shown in Figure 3c, M_S remains largely unaffected by increasing tramp element concentrations, and consequently, shows no significant dependence on PAG size as well. Several empirical formulae are available to estimate the effect of chemical composition on M_s.[43] These formulae suggest that C and Mn content exhibit the most significant influence, seemingly overshadowing the effect of the low concentrations of tramp elements such as Cr, Mo, Cu, and Ni in both the trial alloy with medium and high levels of tramp elements. Another possibility is that the C content of the investigated steel is already too high to have an influence on M_S, as this effect is less pronounced with increasing C content.[16] Nevertheless, it can be inferred that the solute drag effect, while contributing to a reduction in PAG size, is not sufficiently pronounced to influence the phase transformation behavior to a significant extent. This challenges conventional assumptions about grain size effects and indicates that compositional influences, particularly boundary segregation effects, dominate over kinetic considerations in this context.

4.3. Potential Challenges for Alloy Design

In the transition toward CO_2-reduced steel production, the steel industry faces several significant challenges. One of the key issues arises from the increased use of scrap in EAF processes, which results in a feedstock composition heavily influenced by the intended steel grade. This is particularly critical for steel types with stringent limits on allowable impurity levels. Oxygen injection during processing creates oxidizing conditions, but metallic impurities such as Cu, Sn, Cr, and Ni cannot be effectively eliminated because they have a higher nobility than Fe. Therefore, the control of these elements relies on careful adjustment of the charge composition, often achieved through the targeted addition of low-residual materials such as direct reduced iron (DRI) or pig iron.[44] Consequently, it is crucial to understand the tolerance of specific steel grades to impurity levels, particularly in the form of tramp elements, before such additions begin to significantly alter key characteristics, such as phase transformation behavior during processing. The current study demonstrates that the addition of tramp elements promotes displacive phase transformations (Figure 2). However, a distinction remains between the medium level and the high level alloying conditions, indicating a concentration-dependent effect. This suggests that regulating the concentration of tramp elements through controlled dilution of scrap with DRI or pig iron could allow for compositions that do not significantly alter phase transformation behavior. Achieving this, however, requires a comprehensive understanding of how individual and combined tramp elements influence phase transformations. The results of the present work represent an important first step in this direction.

An alternative approach to mitigate displacive transformations induced by elevated tramp element concentrations is to modify process parameters, such as reducing the cooling rate during processing. However, in the case of pearlitic microstructures, slower cooling rates result in increased interlamellar spacing, which is typically associated with a reduction in mechanical strength.[45] This adverse effect can be mitigated by making use of the interlamellar spacing, reducing the influence of specific tramp elements.[33,34] Therefore, while adjusting cooling conditions may offer a degree of control, it also involves trade-offs that must be carefully considered in relation to the targeted material properties.

A detailed understanding of the effects of tramp elements may enable their strategic use in future alloy and process design. For instance, they could potentially be exploited to tailor the hardenability of a given steel grade or to benefit from the associated refinement of the PAG size.[46,47] Moreover, the concept of counteralloying could be applied by compensating for the presence of tramp elements through tailored adjustments in the concentrations of other key alloying elements, such as reducing the carbon content, while still achieving the desired hardenability.[48] This approach could offer new flexibility in alloy design under increasingly variable scrap-based compositions.

5. Summary and Conclusion

In this work, a hypoeutectoid wire rod steel was utilized to examine the effect of tramp elements on the microstructural evolution, particularly focusing on the formation of displacive phases. The heat treatment behavior of the alloy from BF production was compared to that of trial alloys with intentionally increased tramp element concentrations.

Although all three investigated alloys had similar ferritic-pearlitic initial microstructures and were subjected to identical heat treatments, the alloys with higher amount of tramp elements showed significantly higher amounts of martensite after cooling to RT. Also dilatometry curves showed a clear kink at the M_s temperature for the alloy with high level of tramp elements. Furthermore, continuous shift of austenite-to-pearlite transformation to lower temperatures with increasing austenite-stabilizing tramp element concentrations (Cu, Ni, Co, and N) is demonstrated.

Hardness measurements revealed that alloys with higher concentrations of tramp elements exhibited increased hardness levels. This enhancement in hardness can be most likely attributed to solid solution strengthening, which could alter the conditions for phase transformations.

Detailed SEM analysis revealed that the evolved displacive microstructural constituent, which is promoted due to the addition of tramp elements, not only consists of martensite but also contains fractions of bainite as well as RA.

The HE-XRD technique was employed to monitor the microstructural evolution throughout the entire heat treatment process. While no significant differences were observed during heat treatment itself, a clear trend emerged after the process was completed. Specifically, the amount of RA increased proportionally with the concentration of tramp elements. This confirms that the presence of these elements influences the stability of RA and its evolution alongside martensite.

Observations using HTLSCM further reinforced the conclusion that increasing tramp element concentrations promote martensite formation. It was found that the PAG size at 1100 °C decreased with increasing tramp element content. This grain refinement is likely due to a solute drag effect, where tramp elements restrict grain boundary movement during high-temperature exposure. The segregation of elements, such as Sn, Cu, or P can suppress the nucleation and reduce the growth rate of diffusion-controlled phases, such as ferrite or pearlite.

Ultimately, the alteration in phase transformation behavior results from the interplay between changes in chemical composition and the consequent modification of PAG size. The enrichment of tramp elements expands the martensite region in CCT diagrams and lowers critical cooling rates for displacive transformations. This leads to a higher martensite fraction in alloys with increased tramp element content. Simultaneously, these elements are very likely contributing to a reduction in PAG size. This refinement of grain structure usually promotes the formation of pearlite by increasing the density of nucleation sites. Consequently, while the solute drag effect reduces PAG size, its impact on phase transformation behavior is minimal or not significant enough to induce substantial changes.

In summary, the observed reduction in PAG size due to increased concentrations of tramp elements has a minor effect on phase transformation behavior. In contrast, the influence of elements like Cu and Sn on PAG boundary energy as well as the austenite-stabilizing effect of Cu, Ni, Co, and N plays a much more significant role in altering phase transformation behavior. In order to clearly distinguish the effects of chemical composition and PAGs, future investigations need to include alloys with the same tramp element concentrations but varying PAG sizes or vice versa. Nonetheless, this study provides clear evidence of the influence of tramp elements on phase transformation behavior and PAG development.

Supporting Information

Supporting Information is available from the Wiley Online Library or from the author.

Acknowledgements

The authors gratefully acknowledge the financial support by the Austrian Federal Ministry for Digital and Economic Affairs, the National Foundation for Research, Technology and Development, the Christian Doppler Forschungsgesellschaft (CDG), and the valuable collaboration of the industrial partner, voestalpine Forschungsservicegesellschaft, whose expertise has greatly enriched this work.

Conflict of Interest

The authors declare no conflict of interest.

Author Contributions

Lukas Hatzenbichler: conceptualization; investigation; methodology; visualization; project administration; writing—original (draft). **Marek Gocnik**: investigation; visualization; writing—review & editing. **Phillip Haslberger**: conceptualization; resources; writing—review & editing. **Matthew Galler**: resources; writing—review & editing. **Andreas Stark**: resources. **Oleksandr Glushko**: writing—review & editing. **Jozef Keckes**: resources; supervision; writing—review & editing. **Ronald Schnitzer**: resources; supervision; writing—review & editing.

Data Availability Statement

The data that support the findings of this study are available from the corresponding author upon reasonable request.

Keywords

high-energy X-ray diffraction, high-temperature laser scanning confocal microscope, phase transformations, prior austenite grains, tramp elements

Received: February 25, 2025
Revised: May 12, 2025

[1] R. Maier, T. Gerres, A. Tuerk, F. Mey, *Glob. Environ. Change* **2024**, *86*, 102846.
[2] I. Daigo, K. Tajima, H. Hayashi, D. Panasiuk, K. Takeyama, H. Ono, Y. Kobayashi, K. Nakajima, T. Hoshino, *ISIJ Int.* **2021**, *61*, 498.
[3] D. Raabe, M. Jovičević-Klug, D. Ponge, A. Gramlich, A. Kwiatkowski Da Silva, A. N. Grundy, H. Springer, I. Souza Filho, Y. Ma, *Annu. Rev. Mater. Res.* **2024**, *54*, 247.
[4] K. E. Daehn, A. C. Serrenho, J. Allwood, *Metall. Mater. Trans. B Process Metall. Mater. Process. Sci.* **2019**, *50*, 1225.
[5] S. Bell, B. Davis, A. Javaid, E. Essadiqi, *Final Rep. Nat. Resour. Can.* **2006**, 1.
[6] V. A. Malyshevskii, T. G. Semicheva, E. I. Khlusova, *Met. Sci. Heat Treat.* **2001**, *43*, 331.
[7] V. K. Devra, J. Maity, *Philos. Mag. Lett.* **2020**, *100*, 245.
[8] M. Kern, M. Bernhard, Y.-B. Kang, C. Bernhard, *Acta Mater.* **2024**, *269*, 119826.
[9] N. Fuchs, P. Krajewski, C. Bernhard, *Monatshefte* **2015**, *160*, 214.
[10] H. I. Aaronson, *Proeutectoid Ferrite Proeutectoid Cem. React.* in Decomposition of Austenite by Diffusional Processes, V. F. Zackay and H. I. Aaronson, Eds. New York: Interscience Publishers **1962**, *387*.
[11] M. M. Aranda, B. Kim, R. Rementeria, C. Capdevila, C. G. De Andrés, *Metall. Mater. Trans. A* **2014**, *45*, 1778.
[12] J.-Y. Yan, J. Ågren, J. Jeppsson, *Metall. Mater. Trans. A* **2020**, *51*, 1978.
[13] H. Ohtsuka, G. Ghosh, K. Nagai, *ISIJ Int.* **1997**, *37*, 296.
[14] C. Celada-Casero, J. Sietsma, M. J. Santofimia, *Mater. Des.* **2019**, *167*, https://doi.org/10.1016/j.matdes.2019.107625.
[15] C. García De Andrés, *Mater. Charact.* **2002**, *48*, 101.
[16] C. Capdevila, F. G. Caballero, C. García De Andrés, *Mater. Sci. Technol.* **2003**, *19*, 581.
[17] S.-J. Lee, K.-S. Park, *Metall. Mater. Trans. A* **2013**, *44*, 3423.
[18] S. M. C. Van Bohemen, J. Sietsma, *Mater. Sci. Technol.* **2009**, *25*, 1009.
[19] J. Moravec, M. Mičian, M. Málek, M. Švec, *Materials* **2022**, *15*, 4637.
[20] E.-96 ASTM, Standard test methods for determining average grain size, ASTM Int. West Conshohocken PA USA, **2004**.
[21] A. Standard, ASTM E92–17, 2017a, Standard test methods for vickers hardness and knoop hardness of metallic materials, West Conshohocken PA USA ASTM Int **2017**.
[22] G. Ashiotis, A. Deschildre, Z. Nawaz, J. P. Wright, D. Karkoulis, F. E. Picca, J. Kieffer, *J. Appl. Crystallogr.* **2015**, *48*, 510.

[23] R. Kawulok, I. Schindler, P. Kawulok, J. Dänemark, P. Opěla, S. Rusz, Study of phase transformation of medium carbon steel after hot plastic deformation, in: Solid State Phenom., Trans Tech Publications Ltd **2017**, pp. 599–602, https://doi.org/10.4028/www.scientific.net/SSP.258.599.

[24] H. K. D. H. Bhadeshia, *Mater. Sci. Eng. A* **1999**, *273–275*, 58.

[25] T. Furuhara, T. Moritani, K. Sakamoto, T. Maki, Substructure and crystallography of degenerate pearlite in an Fe-C binary alloy, in: Mater. Sci. Forum, Trans Tech Publ **2007**, pp. 4832–4837, https://www.scientific.net/MSF.539-543.4832 (accessed July 25, 2024).

[26] J. Kundrák, Z. Gácsi, K. Gyáni, V. Bana, G. Tomolya, *Int. J. Adv. Manuf. Technol.* **2012**, *62*, 457.

[27] V. A. Esin, B. Denand, Q. L. Bihan, M. Dehmas, J. Teixeira, G. Geandier, S. Denis, T. Sourmail, E. Aeby-Gautier, *Acta Mater.* **2014**, *80*, 118.

[28] S. Gollapudi, S. Gollapudi, OpenCV with python, Learn Comput. Vis. Using OpenCV Deep Learn. CNNs RNNs, Berkeley, CA, **2019**, 31–50.

[29] N. Fuchs, C. Bernhard, *Mater. Today Commun.* **2021**, *28*, https://doi.org/10.1016/j.mtcomm.2021.102468.

[30] J. Collins, M. Taylor, A. L. Scarlett, E. J. Palmiere, E. J. Pickering, *Mater. Charact.* **2024**, *208*, 113656.

[31] C. Garcıá De Andrés, F. G. Caballero, C. Capdevila, D. San Martıń, *Mater. Charact.* **2002**, *49*, 121.

[32] G. Ghosh, G. B. Olson, *Acta Metall. Mater.* **1994**, *42*, 3361.

[33] C. Houpert, V. Lanteri, J. M. Jolivet, M. Guttmann, J. R. Birat, M. Jallon, M. Confente, *Rev. Metall. Cah. Inf. Tech.* **1997**, *94*, 1369.

[34] G. T. Eavenson, Effects of copper on the metallurgical, mechanical, and fracture properties of 0.90 carbon rail steels, Colorado School of Mines, PhD Theses, **2015**.

[35] H.-J. Bargel, G. Schulze, *Grundlagen Der Metall- Und Legierungskunde, Werkstoffkunde*, Springer Vieweg, 11th edition **2012**, 1–80. https://doi.org/10.1007/978-3-642-17717-0.

[36] S. H. Ryu, M. S. Kim, Y. S. Lee, J. T. Kim, J. Yu, B. J. Lee, The effects of carbon and austenite stabilizing elements (Co, Cu, Ni and Mn) on the microstructural changes and the creep rupture strength in 9-12% Cr ferritic heat resistant steels, in: AM-EPRI 2004, ASM International, **2004**, pp. 1280–1298. https://doi.org/10.31399/asm.cp.am-epri-2004p1280.

[37] D. T. Pierce, D. R. Coughlin, K. D. Clarke, E. De Moor, J. Poplawsky, D. L. Williamson, B. Mazumder, J. G. Speer, A. Hood, A. J. Clarke, *Acta Mater.* **2018**, *151*, 454.

[38] Z. Xu, J. Li, X. Shen, T. Allam, S. Richter, W. Song, W. Bleck, *Metals* **2021**, *11*, 1888.

[39] A. K. Cianelli, H. C. Feng, A. H. Ucisik, C. J. McMahon, *Metall. Trans. A* **1977**, *8*, 1059.

[40] B. Mehta, X. Yang, L. Höglund, W. Mu, P. Hedström, *J. Sustain. Metall.* **2025**, https://doi.org/10.1007/s40831-025-01093-4.

[41] X. Xu, T.-F. Chung, S. Hu, Q. Zhu, J. Fu, J.-R. Yang, Q. Tian, *J. Mater. Res. Technol.* **2022**, *20*, 1172.

[42] L. Fan, R. Dong, S. Qiu, L. Xiang, G. Tang, *J. Supercond. Nov. Magn.* **2014**, *27*, 1959.

[43] C. Y. Kung, J. J. Rayment, *Metall. Trans. A* **1982**, *13*, 328.

[44] J. Madias, *Electric Furnace Steelmaking, In: Treatise Process Metall.*, Industrial Processes, chapter 1.5 Elsevier **2024**, vol. *3*, pp. 243–265, https://doi.org/10.1016/B978-0-323-85373-6.00021-1.

[45] A. R. Marder, B. L. Bramfitt, *Metall. Trans. A* **1976**, *7*, 365.

[46] X. Li, G. Lu, Q. Wang, J. Zhao, Z. Xie, R. D. K. Misra, C. Shang, *Metals* **2021**), *12*, 28.

[47] S. A. Khan, M. A. Islam, *J. Mater. Eng. Perform.* **2007**, *16*, 80.

[48] A. M. Llopis, Effect of Alloying Elements in Steels on the Kinetics of the Austenite to Bainite transformation, Lawrence Berkeley National Laboratory, LBNL Report #: LBL-4555, retrieved from **1975**. https://escholarship.org/uc/item/6gf4f53v.

[49] Y.-C. Chen, *Biostat. Epidemiol.* **2017**, *1*, 161.